Icarus **174** (2), 475–485, 2005
http://icarus.cornell.edu/
— Authors' final version —

Influence of ice rheology and dust content on the dynamics of the north-polar cap of Mars

Ralf Greve (1, 2) and Rupali A. Mahajan (3)

(1) Institute of Low Temperature Science, Hokkaido University, Kita-19, Nishi-8, Kita-ku, Sapporo 060-0819, Japan

(2) Department of Mechanics, Darmstadt University of Technology, Hochschulstraße 1, D-64289 Darmstadt, Germany

(3) Max Planck Institute for Solar System Research*, Max-Planck-Straße 2, D-37191 Katlenburg-Lindau, Germany

* Former Max Planck Institute for Aeronomy

February 28, 2005

Correspondence to: R. Greve (greve@lowtem.hokudai.ac.jp)

Abstract

The evolution and dynamics of the north-polar cap (residual-ice-cap/layered-deposits complex) of Mars is simulated with a thermomechanical ice-sheet model. We consider a scenario with ice-free initial conditions at 5 Ma before present due to the large obliquities which prevailed prior to this time. The north-polar cap is then built up to its present shape, driven by a parameterized climate forcing (surface temperature, surface mass balance) based on the obliquity and eccentricity history. The effects of different ice rheologies and different dust contents are investigated. It is found that the build-up scenarios require an accumulation rate of approximately 0.15–0.2 mm a^{-1} at present. The topography evolution is essentially independent of the ice dynamics due to the slow ice flow. Owing to the uncertainties associated with the ice rheology and the dust content, flow velocities can only be predicted within a range of two orders of magnitude. Likely present values are of the order of 0.1–1 mm a^{-1}, and a strong variation over the climatic cycles is found. For all cases, computed basal temperatures are far below pressure melting.

1 Introduction

One of the most prominent features of the Martian surface are the polar ice caps. While the seasonal caps consist of only some ten centimeters of CO_2 snow which sublimes into the atmosphere during the respective summer season, the smaller residual caps poleward of approximately 80°N/S are underlain by massive topographic structures known as the polar layered deposits (Thomas et al. 1992). Following the terminology of recent publications (e.g. Johnson et al. 2000, Byrne and Murray 2002, Greve et al. 2004), the complexes composed of the residual caps and the underlying layered deposits are referred to as the north- and south-polar cap (NPC/SPC), respectively. The Mars Orbiter Laser Altimeter (MOLA) measurements of the Mars Global Surveyor (MGS) spacecraft have provided a very precise mapping of the surface topographies of the polar caps (Smith et al. 1999, Zuber et al. 1998).

As far as it is known, the NPC and SPC are the largest water reservoirs on Mars. Further constituents may be dust, CO_2 ice and CO_2 clathrate hydrate. The polar caps are active components of the Martian climate system which interact with the atmosphere thermally, orographically and by condensation and sublimation processes of water vapour. Previous studies (Greve 2000b, Greve et al. 2003, Hvidberg 2003, Hvidberg and Zwally 2003, Greve et al. 2004) indicate that the NPC is a dynamic ice mass which shows glacial flow of the order of 1 mm a^{-1} at present. Its present topography is the

result of the climatic history over at least the last millions of years, which was probably characterized by climate cycles as a consequence of strong, quasi-periodic variations of the orbital parameters obliquity, eccentricity and precession on time-scales of 10^5–10^6 years (Laskar et al. 2002). This idea is supported by the light-dark layered deposits of both polar caps indicating a strongly varying dust content of the ice due to varying atmospheric conditions.

In this study, the dynamic and thermodynamic evolution of the NPC will be simulated with the ice-sheet model SICOPOLIS. The boundary conditions of surface accumulation, ablation and temperature are derived directly from the solar-insolation history by applying the Mars Atmosphere-Ice Coupler MAIC developed by Greve et al. (2004). Due to the high obliquities between ten and five million years before present (Ma BP) and subsequent high sublimation rates (Jakosky et al. 1993), the NPC did probably not survive this period. Therefore, we assume ice-free conditions during that time and consider transient scenarios in which the NPC is formed during the last five million years. A large uncertainty in model studies of that kind results from the poorly constrained rheological properties of the ice and the unknown dust content. Therefore, we will look systematically into the influence of these two aspects on the evolution of ice topography and glacial flow of the ice body.

2 Framework of the simulations

2.1 Ice-sheet model SICOPOLIS

The dynamic/thermodynamic ice-sheet model SICOPOLIS used for the simulations of this study was developed in the mid-1990's for terrestrial applications. Since then, it was applied to numerous problems of past, present and future glaciation on Earth (see Greve 2000a, and references therein). Adaptation to the Martian NPC was performed by Greve (2000b), Greve et al. (2003, 2004). Main features of the model are:

- Three-dimensional, large-scale, polythermal ice-sheet model, applies the shallow-ice approximation (Hutter 1983, Morland 1984).
- Computation of the temporal evolution of the field quantities (i) ice extent and thickness, (ii) flow velocity, (iii) temperature, (iv) water content, (v) age.
- Coupled lithosphere module accounting for local isostatic displacement and temperature.

- External forcing specified by (i) mean annual air temperature at the ice surface, (ii) net surface mass balance (ice accumulation minus ablation), (iii) global sea level (not relevant for Martian applications in the recent past), (iv) geothermal heat flux.

In the version for the Martian NPC, all computations are carried out in a stereographic plane with standard parallel 71°N. The model domain is a square of size 1800 km × 1800 km, centered at the north pole. The horizontal resolution is 20 km, the vertical resolution 51 grid points in the cold-ice column, 11 grid points in the temperate-ice column (if existing) and 11 grid points in the lithosphere column. Standard physical parameters are listed in Table 1; they agree with those used previously by Greve et al. (2004). For more details please refer to this study.

Quantity	Value
Martian gravity acceleration, g_0	$3.72\,\mathrm{m\,s^{-2}}$
Density of ice, ρ_i	$910\,\mathrm{kg\,m^{-3}}$
Heat conductivity of ice, κ_i	$9.828\,e^{-0.0057\,T[\mathrm{K}]}\,\mathrm{W\,m^{-1}K^{-1}}$ *
Specific heat of ice, c_i	$(146.3 + 7.253\,T[\mathrm{K}])\,\mathrm{J\,kg^{-1}K^{-1}}$ *
Latent heat of ice, L	$335\,\mathrm{kJ\,kg^{-1}}$
Clausius-Clapeyron constant for air-saturated glacier ice, β	$9.8 \times 10^{-8}\,\mathrm{K\,Pa^{-1}}$
Melting point at zero pressure, T_0	273.15 K
Density of crustal material, ρ_c	$2900\,\mathrm{kg\,m^{-3}}$
Heat conductivity of crustal material, κ_c	$2.5\,\mathrm{W\,m^{-1}\,K^{-1}}$
Geothermal heat flux, q_geo	$35\,\mathrm{mW\,m^{-2}}$
Fraction of isostatic compensation, f_iso	0.65
Isostatic time lag, τ_iso	3000 a
Asthenosphere density, ρ_a	$3300\,\mathrm{kg\,m^{-3}}$
Density × specific heat of the lithosphere, $\rho_\mathrm{r} c_\mathrm{r}$	$2000\,\mathrm{kJ\,m^{-3}K^{-1}}$
Heat conductivity of the lithosphere, κ_r	$3\,\mathrm{W\,m^{-1}K^{-1}}$

Table 1: Standard physical parameters of the ice-sheet model SICOPOLIS. * T[K]: temperature T measured in K.

2.2 Climatic forcing

The climatic forcing for the NPC simulations consists of the surface air temperature and the surface mass balance prescribed as functions of space and time. The parametrization employed here is based on the ten-million-year history of Martian obliquity θ (Fig. 1,

top panel) and eccentricity e (not shown) by Laskar et al. (2002). From these data, the climatic forcing is derived by using the Mars Atmosphere-Ice Coupler MAIC described in detail by Greve et al. (2004). Therefore, the procedure is only sketched here briefly. In Table 2 the relevant parameters are compiled.

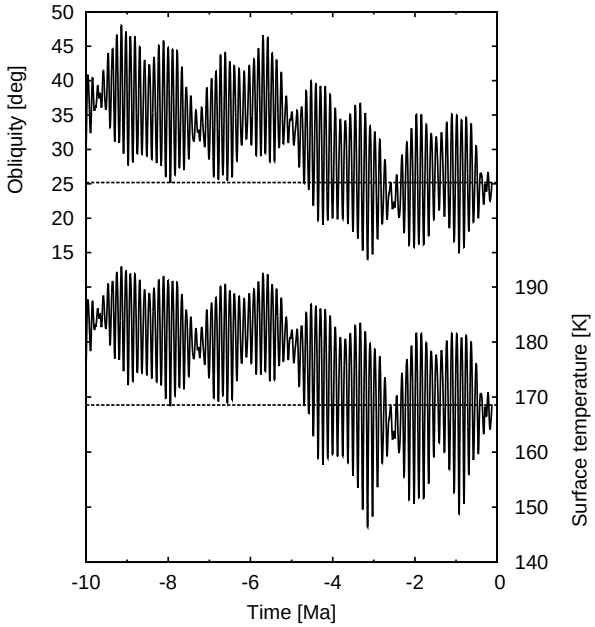

Figure 1: Obliquity θ (top, by Laskar et al. 2002) and mean annual surface temperature at the north pole T_{np} (bottom) for the last ten million years. Dashed lines indicate present values.

Quantity	Value
Solar flux at average distance Sun – Mars, I_{s}	$590\,\mathrm{W\,m^{-2}}$
Albedo, A_{m}	0.43
Emissivity, ε	1
Stefan-Boltzmann constant, σ_{SB}	$5.67 \times 10^{-8}\,\mathrm{W\,m^{-2}\,K^{-4}}$
Co-latitude temperature coefficient, c_{s}	$2.25\,\mathrm{K\,(^{\circ}co\text{-}lat)^{-1}}$
Latent heat for sublimation of water ice, λ	$2860\,\mathrm{kJ\,kg^{-1}}$
Material gas constant for water, R_{m}	$461.5\,\mathrm{J\,kg^{-1}\,K^{-1}}$
Present atmospheric reference temperature, T^0_{ref}	173 K
Equilibrium-line distance, d_{el}	550 km
Mass-balance-gradient parameter, l_{g}	400 km

Table 2: Standard physical parameters of the atmosphere-ice coupler MAIC.

The mean annual insolation at the north pole, $I^{\mathrm{in}}_{\mathrm{np}}$, is computed as a function of time from the obliquity and eccentricity data. This quantity is balanced with the outgoing mean annual longwave radiation, which is related to the mean annual surface tempera-

ture at the north pole, $T_{\rm np}$, by the Stefan-Boltzmann law. This yields

$$T_{\rm np}(t) = \left(\frac{I^{\rm in}_{\rm np}(t)\,(1 - A_{\rm m})}{\varepsilon \sigma_{\rm SB}} \right)^{1/4}, \tag{1}$$

where t is the time (from JED 2440400.5 or 28 June 1969), $A_{\rm m}$ the mean albedo of the NPC, ε the emissivity and $\sigma_{\rm SB}$ the Stefan-Boltzmann constant (Fig. 1, bottom panel; computed with the parameters of Table 2). For any position off the pole, the surface temperature $T_{\rm s}$ is then

$$T_{\rm s}(\tilde{\phi}, t) = T_{\rm np}(t) + c_{\rm s}\,\tilde{\phi}, \tag{2}$$

where $\tilde{\phi}$ is the co-latitude (angular distance from the pole) and $c_{\rm s}$ the co-latitude temperature coefficient. Like in the simulations by Greve et al. (2004) no explicit dependence on surface elevation is considered.

The accumulation rate $a^+_{\rm sat}$ ("saturation accumulation") is computed by assuming proportionality to the water-vapour saturation pressure in the atmosphere. This yields the relation

$$a^+_{\rm sat}(t) = a^+_{\rm sat,0} \exp\left(\frac{\lambda}{R_{\rm m} T^0_{\rm ref}} - \frac{\lambda}{R_{\rm m}(T^0_{\rm ref} + \Delta T_{\rm s}(t))} \right), \tag{3}$$

where $a^+_{\rm sat,0}$ is the present accumulation rate, λ is the latent heat for sublimation/condensation of water ice, $R_{\rm m}$ is the material gas constant for water, $T^0_{\rm ref}$ is the present atmospheric reference temperature and $\Delta T_{\rm s}(t) = T_{\rm np}(t) - T_{\rm np}(0)$ is the surface-temperature anomaly.

From the saturation accumulation (3), the net mass balance $a_{\rm net} = a^+_{\rm sat} - a^-$ (a^-: ablation rate) is derived by the equilibrium-line approach

$$a_{\rm net}(\tilde{\phi}, t) = \min\left[a^+_{\rm sat}(t),\, g(t) \times (d_{\rm el} - d_{\rm np}(\tilde{\phi})) \right], \tag{4}$$

where g is the mass-balance gradient, $d_{\rm np}$ the distance from the pole and $d_{\rm el}$ the distance of the equilibrium line where the net mass balance is equal to zero. For simplicity and lack of better knowledge, $d_{\rm el}$ is assumed to be temporally constant, and a good approximation for it is the mean radius of the present cap. The mass-balance gradient is taken proportional to the accumulation rate,

$$g(t) = \frac{a^+_{\rm sat}(t)}{l_{\rm g}}, \tag{5}$$

where $l_{\rm g}$ is the mass-balance-gradient parameter. For the parameters of Table 2, the net mass balance resulting from Eq. (4) is displayed in Fig. 2.

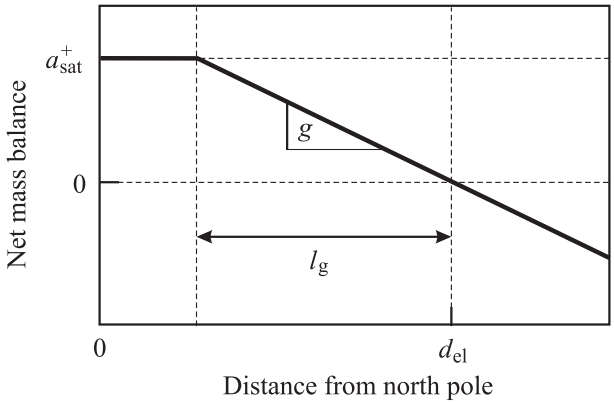

Figure 2: Net mass balance (accumulation-ablation rate) resulting from the parametrization (4) and the parameters of Table 2.

3 Ice rheology

Several forms of a non-linear viscous rheology for the flow of polycrystalline ice for different stress, strain-rate and temperature regimes have been proposed. They have in common to relate the strain-rate tensor $\boldsymbol{D} = \mathrm{sym}\,\mathrm{grad}\,\boldsymbol{v}$ (velocity $\boldsymbol{v}$) to the Cauchy stress deviator $\boldsymbol{t}^{\mathrm{D}}$, and can be subsumed as

$$\boldsymbol{D} = EA(T,P)\frac{\sigma^{n-1}}{d^p}\,\boldsymbol{t}^{\mathrm{D}}, \tag{6}$$

where $\sigma = [\mathrm{tr}\,(\boldsymbol{t}^{\mathrm{D}})^2/2]^{1/2}$ is the effective stress, n is the stress exponent, d is the grain size and p is the grain-size exponent (e.g. Paterson 1994, Durham et al. 1997, Goldsby and Kohlstedt 1997, van der Veen 1999). The flow rate factor $A(T,P)$ depends via the Arrhenius law

$$A(T,P) = A_0\, e^{-(Q+PV)/RT} \tag{7}$$

on the absolute temperature T and the pressure P, where A_0 is the preexponential constant, Q is the activation energy, V is the activation volume and $R = 8.314$ J mol^{-1} K^{-1} is the universal gas constant. The flow enhancement factor E is equal to unity for pure ice and can deviate from unity due to the softening or hardening effect of impurities in the ice.

Since appropriate values for the activation volume V are poorly constrained and the pressure effect is very small for typical thicknesses of ice sheets and caps, we account for it in an approximate way by setting $V = 0$ and measuring the temperature relative to the pressure melting point $T_{\mathrm{m}} = T_0 - \beta P$ instead ($T_0 = 273.15$ K is the melting point at zero pressure, and β is the Clausius-Clapeyron constant for air-saturated glacier ice).

This yields the simplified flow rate factor

$$A(T') = A_0\, e^{-Q/RT'}, \tag{8}$$

which depends now exclusively on the homologous temperature $T' = T - T_\mathrm{m} + T_0 = T + \beta P$ (Rigsby 1958, Paterson 1994, van der Veen 1999).

By introducing the effective strain rate $\delta = (\mathrm{tr}\,\boldsymbol{D}^2/2)^{1/2}$, the inverse form of the general power law (6) with the flow rate factor (8) is readily obtained as

$$\boldsymbol{t}^\mathrm{D} = E_\mathrm{s} B(T') \frac{d^{p/n}}{\delta^{1-1/n}}\, \boldsymbol{D} \tag{9}$$

(van der Veen 1999). Here, $E_\mathrm{s} = E^{-1/n}$ denotes the stress enhancement factor, and $B(T') = [A(T')]^{-1/n}$ is the associated rate factor.

For terrestrial ice, the well-established Glen's flow law [which actually goes back to Nye (1953) in the general tensorial form] uses the stress exponent $n = 3$, the grain-size exponent $p = 0$ and for the temperature range $T' \leq 263$ K the preexponential constant $A_0 = 3.985 \times 10^{-13}\ \mathrm{s^{-1}\,Pa^{-3}}$ and the activation energy $Q = 60\ \mathrm{kJ\,mol^{-1}}$ (Paterson 1994). The rheology defined by these parameters describes the grain-size-independent flow mechanism of dislocation creep, which prevails in terrestrial glaciers and ice sheets. The flow enhancement factor for ice formed during glacial periods is often set to $E = 3$, interpreted as the softening influence of very small amounts of fine dust, approximately $1\ \mathrm{mg\,kg^{-1}}$ with particle sizes of 0.1 to $2\,\mu$m (Hammer et al. 1985). This softening is attributed to thin films of liquid water which form around the dust particles and lubricate ice deformation. However, at the low temperatures expected in the NPC this effect will not be present, and direct hardening will be the dominant influence of dust (see Sect. 4).

Durham et al. (1997) have proposed an alternative flow law for grain-size-independent dislocation creep, based on laboratory creep tests at a confining pressure of 50 MPa. For the temperature regime $T = 195$–240 K, which corresponds approximately to $T' = 200$–245 K, they report the parameters $n = 4$, $p = 0$, $A_0 = 1.259 \times 10^{-19}\ \mathrm{s^{-1}\,Pa^{-4}}$ and $Q = 61\ \mathrm{kJ\,mol^{-1}}$.

However, it is not clear whether dislocation creep is the predominant creep mechanism for the low temperatures and low strain rates in the Martian caps. There is evidence that other, grain-size-dependent flow mechanisms like grain-boundary sliding become favoured instead (Goldsby and Kohlstedt 1997). These can be described by the parameters $n = 1.8$, $p = 1.4$, $A_0 = 6.20 \times 10^{-14}\ \mathrm{s^{-1}\,Pa^{-1.8}\,m^{1.4}}$ and $Q = 49\ \mathrm{kJ\,mol^{-1}}$ (see also Nye 2000).

For this flow law (which will be referred to as "G & K" in the following) an upper limit for the grain size d can be obtained by assuming that it is a result of normal grain growth only. From a variety of data for terrestrial polar ice masses and theoretical considerations, the growth rate

$$\frac{\mathrm{d}}{\mathrm{d}t}(d^2) = k \tag{10}$$

was derived, where t is the time and $\mathrm{d}/\mathrm{d}t$ is the material time derivative which follows the motion of the ice particles. The growth-rate parameter k depends on the absolute temperature T via the Arrhenius law

$$k(T) = k_0\, e^{-Q_k/RT}, \tag{11}$$

with the activation energy $Q_k = 42.5$ kJ mol^{-1} and the constant $k_0 = 9.5$ m^2 a^{-1} (Thorsteinsson 1996). As an example, for $T = 173$ K this yields a growth rate of 1.40 mm^2 Ma^{-1}. By assuming a typical age of millions of years for the ice at depth (cf. Greve et al. 2004), a reasonable range for the grain size follows as $d = 1 \ldots 10$ mm.

The relative contributions of the several flow laws can be estimated as follows. For simple shear in the x-z plane and $E = 1$, Eq. (6) reduces to

$$\dot\gamma = 2A(T')\frac{\tau^n}{d^p}, \tag{12}$$

where $\tau = t^{\mathrm{D}}_{xz}$ is the shear stress and $\dot\gamma = \partial v_x/\partial z = 2D_{xz}$ is the shear rate. Figure 3 shows the shear rates resulting from Eq. (12) for the stress range from 10 kPa to 1 MPa and for the temperature $T' = 200$ K [which is typical for the near-basal ice of the NPC; see e.g. Greve et al. (2004)]. This makes evident that the relative contributions of the different flow laws vary strongly. For very low stresses, grain-size dependent flow with a low stress exponent dominates, whereas for higher stresses dislocation creep with a higher stress exponent becomes more important. With the ice density ρ_{i}, the Martian gravity acceleration g_0 (Table 1), the thickness $H = 3$ km and the mean slope $\alpha = H/R$ (radius $R = 550$ km), a representative shear stress τ^* follows as $\tau^* = \rho_{\mathrm{i}} g_0 H\alpha \approx 55.4$ kPa. For $\tau = \tau^*$, the shear rates decrease by roughly an order of magnitude between subsequent values in the order G & K ($d = 1$ mm) > Glen > G & K ($d = 10$ mm) > Durham.

4 Dust content

Satellite imagery shows that parts of the polar caps appear dark, which indicates that they consist of ice with some amount of mixed-in dust. However, for the average volume fraction φ of dust in the ice no quantitative information is available. For modelling stud-

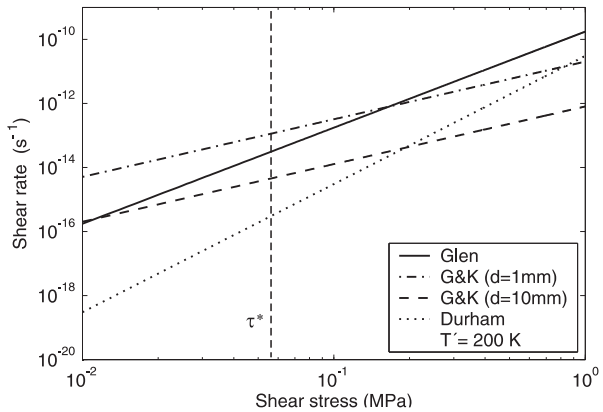

Figure 3: Shear rate $\dot{\gamma}$ vs. shear stress τ for simple shear, computed by Eq. (12) for $T' = 200$ K. Flow laws: Glen ($n = 3$), Durham ($n = 4$), G & K ($n = 1.8$, $p = 1.4$, $d = 1$ mm), G & K ($n = 1.8$, $p = 1.4$, $d = 10$ mm). The representative shear stress τ^* for the NPC (see main text) is indicated.

ies of the polar caps this is a serious problem because the dust content can affect the ice flow via direct hardening, an increasing density and a decreasing heat conductivity which leads to basal warming. Therefore, we compute the density, ρ, and heat conductivity, κ, of the ice-dust mixture as volume-fraction-weighted averages of the values for pure ice and crustal material,

$$\rho = (1-\varphi)\rho_\mathrm{i} + \varphi\rho_\mathrm{c}, \tag{13}$$

$$\kappa = (1-\varphi)\kappa_\mathrm{i} + \varphi\kappa_\mathrm{c}, \tag{14}$$

where ρ_i is the ice density, ρ_c the density of crustal material, κ_i the heat conductivity of ice and κ_c the heat conductivity of crustal material. Values listed in Table 1 are by Greve et al. (2003). Direct hardening is described by a stress enhancement factor $E_\mathrm{s} > 1$ based on laboratory measurements of the deformation of ice-dust compounds,

$$E_\mathrm{s} = e^{b\varphi}, \tag{15}$$

where $b = 2$ (hardening parameter) and $\varphi \leq 0.56$ (Durham et al. 1997). This is equivalent to a flow enhancement factor

$$E = E_\mathrm{s}^{-n} = e^{-nb\varphi}. \tag{16}$$

Hence, for given stress, temperature and grain-size conditions and a stress exponent $n = 3$ a dust content of 10% ($\varphi = 0.1$) leads to an almost twice as hard material ($E = 0.55$) compared to pure ice.

5 The reference simulation

5.1 Set-up

The high average obliquity between 10 and 5 Ma BP (Fig. 1) leads to strongly increased ice sublimation rates (Jakosky et al. 1993). It is highly likely that the NPC did not survive this period (Forget, pers. comm. 2003) and started to build up its present form from ice-free initial conditions at approximately 5 Ma BP. A corresponding ice-free topography was computed by Greve et al. (2004) by a smooth extrapolation of the present ice-free ground surrounding the NPC (Fig. 4).

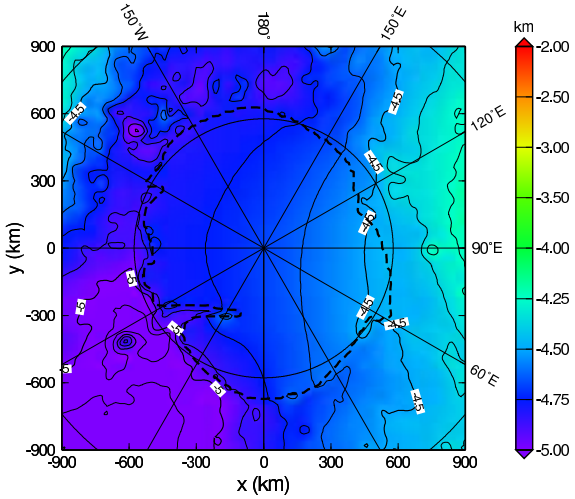

Figure 4: Topography of the equilibrated ground for ice-free conditions (in km relative to the reference geoid) as derived by Greve et al. (2004). The heavy-dashed line indicates the present ice margin derived from the MOLA topography.

For the reference simulation of this study, referred to as run REF, we make use of this scenario. It is assumed that ice-free initial conditions prevail at 5 Ma BP ($t_{\text{init}} = -5$ Ma). The simulation is then run until the present ($t_{\text{final}} = 0$), and the present accumulation rate $a^{+}_{\text{sat},0}$ [see Eq. (3)] is tuned such that the simulated NPC reaches the MOLA value for the maximum surface elevation (with respect to the reference geoid), $h_{\max} = -1.95$ km (Zuber et al. 1998, Smith et al. 1999). Further, Glen's flow law and a vanishing dust content are assumed.

5.2 Results

The above tuning process yields for the present accumulation rate the value $a^{+}_{\text{sat},0} = 0.1575$ mm ice equiv. a^{-1}. From a variety of estimates based on different methods, it is generally agreed that the real value for $a^{+}_{\text{sat},0}$ is of the order of 0.1 mm a^{-1} [in other

words, in the range of $\sim 0.01 \ldots 1$ mm a^{-1}; see the comprehensive discussion by Greve (2000b)], so that our result for $a^{+}_{\mathrm{sat},0}$ can be considered as realistic.

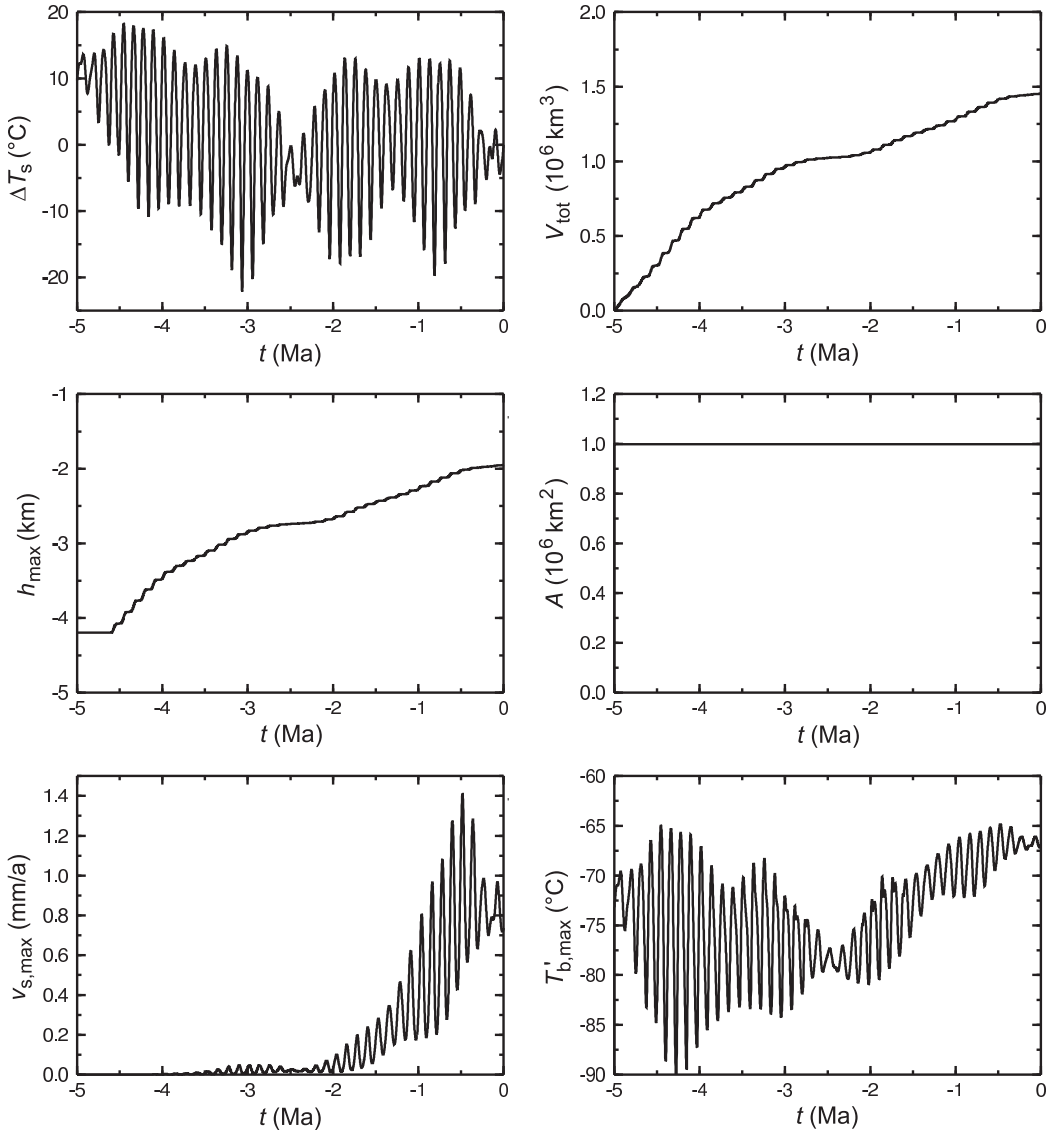

Figure 5: Surface-temperature anomaly ΔT_{s}, total ice volume V_{tot}, maximum surface elevation h_{max}, ice-covered area A, maximum surface velocity $v_{\mathrm{s,max}}$ and maximum basal temperature relative to pressure melting $T'_{\mathrm{b,max}}$ as functions of time for the reference simulation.

Fig. 5 shows the evolution of the surface-temperature anomaly ΔT_{s}, the total ice volume V_{tot}, the maximum surface elevation h_{max}, the ice-covered area A, the maximum surface velocity $v_{\mathrm{s,max}}$ and the maximum basal temperature relative to pressure melting $T'_{\mathrm{b,max}}$. It is evident that V_{tot} and h_{max} increase monotonically over time, and the main 125-ka obliquity cycle which dominates the ΔT_{s} forcing is only reflected as a very small step-like modification. This confirms the earlier finding by Greve et al. (2004) that the NPC topography responds mainly to the long-term average climate conditions. Due to

the non-linear coupling between temperature and accumulation [Eq. (3)], the volume increase does not only depend on the average ΔT_s, but also on its amplitude. This can be seen clearly for the times $t = -2.5$ Ma and $t = 0$ where temperature amplitudes are small and consequently the ice volume is almost constant. The ice-covered area A remains constant for the entire simulation time. This is so because ice-flow velocities are too small to allow the ice cap to enter the ablation zone (negative mass balance), so that it is limited to the accumulation zone (positive mass balance) throughout the model time.

In contrast to the topography parameters V_tot, h_max and A, the dynamic/thermodynamic quantities $v_\mathrm{s,max}$ and $T'_\mathrm{b,max}$ reflect the 125-ka cycle strongly. As for the maximum surface velocity $v_\mathrm{s,max}$, it is interesting that significant ice flow does not start prior to 2 Ma BP, at a time for which the ice volume has already reached two thirds of its present value. This behaviour is a consequence of the nonlinear flow law (stress exponent $n > 1$) which produces extremely low strain rates at low stresses ("pseudoplastic behaviour"). During the last million years, $v_\mathrm{s,max}$ oscillates between some tenths of a millimeter per year and more than one millimeter per year, which is no longer negligible, but still orders of magnitude smaller compared to the flow velocities of terrestrial ice sheets. This is the reason why the topography evolution is essentially unaffected by the internal ice dynamics.

The maximum basal temperature $T'_\mathrm{b,max}$ follows the surface temperature during the first time of the simulation when the ice is still thin. Later, with increasing ice thickness, the amplitudes of the surface signal become more and more attenuated, and $T'_\mathrm{b,max}$ shows an increasing trend because of the thermal insulation of the growing ice cap against the cold surface. The warmest ice temperature throughout the model time is -65°C, which is of course far below melting conditions.

A sequence of surface topography maps at intervals of 1 Ma is presented in Fig. 6. The simulated monotonic growth of the cap, starting from the ice-free state shown in Fig. 4, as well as the constant area over time are clearly visible. Comparison with the MOLA topography shows that the large-scale features of the ice cap (extent, surface elevation, shape) are represented very well. By contrast, small- and medium-scale surface structures like the intriguing spiralling scarps and troughs, the large canyon Chasma Borealis and the detailed margin contour are not reproduced. In view of the simple, axi-symmetric climatic forcing which does not account for local details this is of course no surprise and cannot be expected from our large-scale modelling approach. It may be refined by prescribing different ablation rates for the white areas and the darker scarps (Fisher et al. 2002, Hvidberg 2003, Hvidberg and Zwally 2003); however, this does not answer the open question which mechanisms form these structures in the first place.

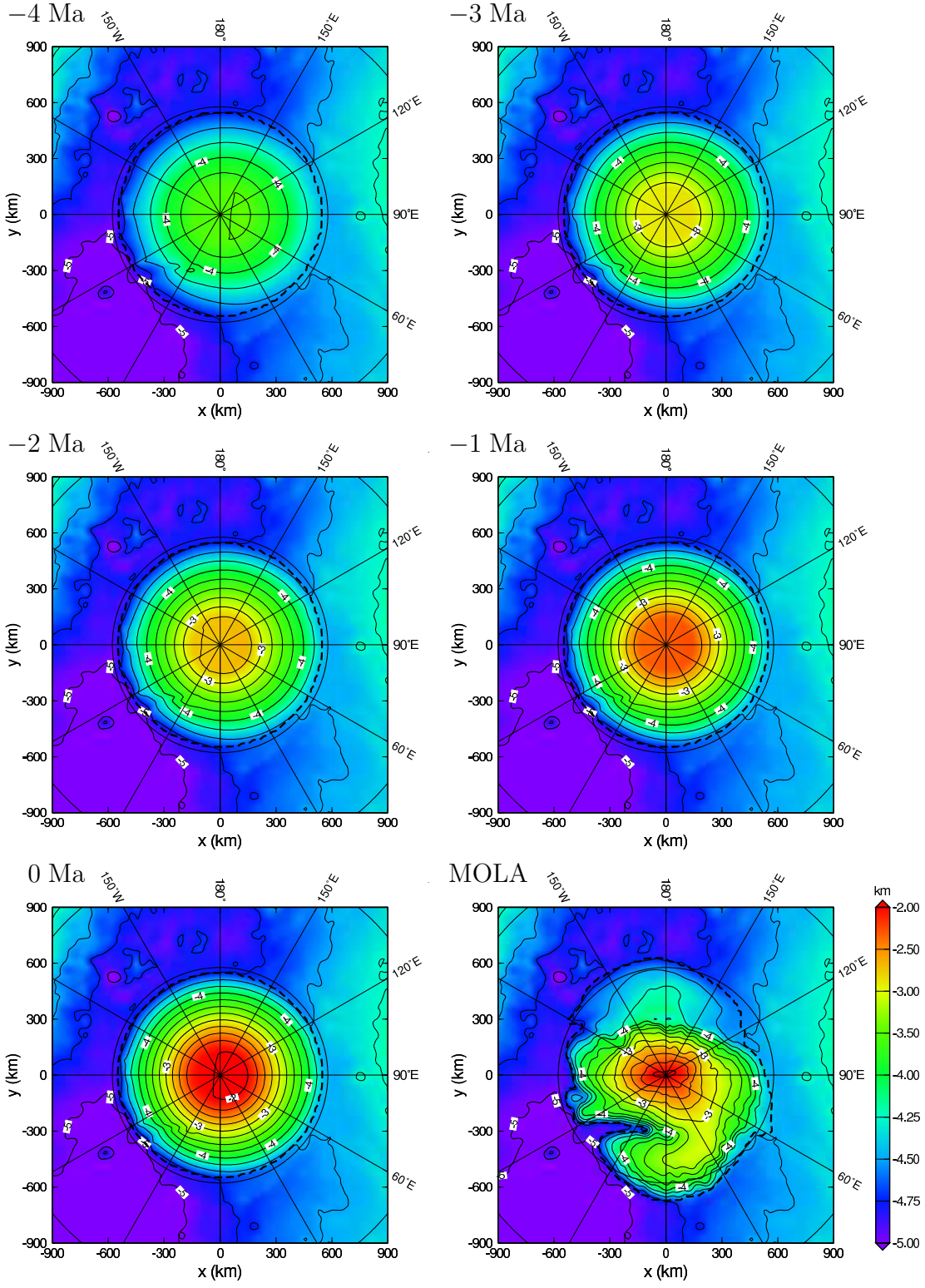

Figure 6: Reference simulation: Surface topography for $t = -4$, -3, -2, -1 and 0 Ma (present), MOLA topography for comparison (in km relative to the reference geoid). Heavy-dashed lines indicate the ice margin.

6 Variation of the flow law and dust content

The influence of the applied flow law and the average dust content on the ice-cap dynamics is now investigated. To this end, two series of simulations have been run. In the first series, Glen's flow law is replaced by Durham's flow law (run DURH) and the flow law by Goldsby and Kohlstedt with grain sizes of 1 mm (run GK01) and 10 mm (run GK10). In the second series, the zero dust content is increased to 10% (run PHI10), 20% (run PHI20), 30% (run PHI30), 40% (run PHI40) and 50% (run PHI50). For all simulations, the present accumulation rate $a^+_{\mathrm{sat},0}$ is adjusted such that the NPC reaches the target value of $h_{\max} = -1.95$ km at $t = 0$. Note that accumulation rates are in ice equivalents for the runs with zero dust content (DURH, REF, GK01, GK10) and in ice+dust equivalents for those with non-zero dust content (PHI10 to PHI50).

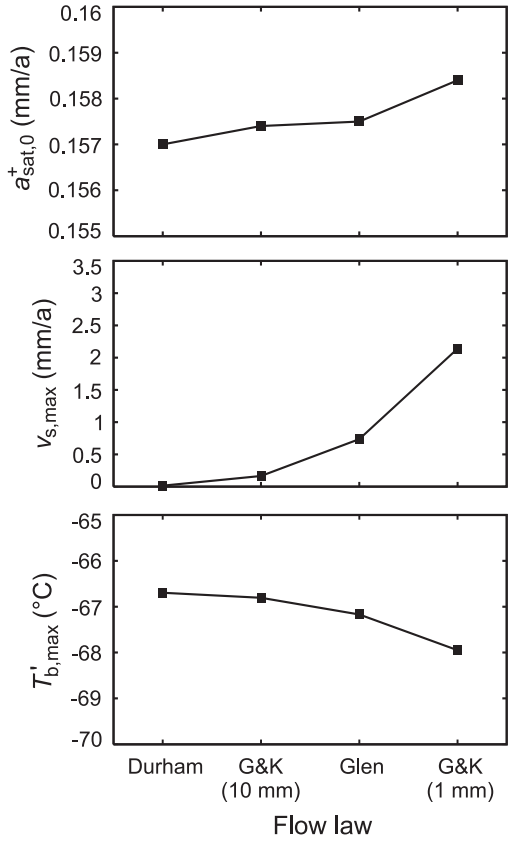

Figure 7: Dependency of the accumulation rate $a^+_{\mathrm{sat},0}$, the maximum surface velocity $v_{\mathrm{s,max}}$ and the maximum basal temperature relative to pressure melting $T'_{\mathrm{b,max}}$ on the applied flow law.

Fig. 7 shows the accumulation rate $a^+_{\mathrm{sat},0}$, the maximum surface velocity $v_{\mathrm{s,max}}$ and the maximum basal temperature relative to pressure melting $T'_{\mathrm{b,max}}$ for the simulation series with varied flow law, arranged for increasing accumulation rates. In fact, $a^+_{\mathrm{sat},0}$ increases only slightly among the simulations, by less than 1%. This small increase

correlates with a drastic increase in $v_{\mathrm{s,max}}$ by approximately two orders of magnitude. The reason for this correlation is that the larger the flow velocities are, the more ice is transported from the interior regions towards the margin, and the more accumulation is required to build up the ice cap to a given surface elevation within a given time-span. However, the flow velocities are always very small (the largest value of 2.14 mm a^{-1} is taken for run GK01), and therefore this dynamic influence on the accumulation rate is not significant. The sequence of simulations with increasing flow velocity, DURH < GK10 < REF < GK01, is the same as already described in Sect. 3 in terms of shear rates of a simple-shear experiment (see also Fig. 3).

Along with the increasing flow velocities, the basal temperatures decrease. This is so because more ice flow entails enhanced advection of cold surface ice downward and outward and therefore cools the lower parts of the NPC. Again, the range of $T'_{\mathrm{b,max}}$ is small due to the small absolute values of the flow velocities, with a difference of slightly more than 1°C between the extremes DURH and GK01. Owing to the exponential dependence of the flow rate factor (8) on T', this cooling produces a slight negative feedback for the increasing ice flow. This explains why the simulated values for $v_{\mathrm{s,max}}$ vary by "only" two orders of magnitude among the simulations, whereas in the simple-shear experiment of Sect. 3, the shear rates show a variation of almost three orders of magnitude.

In Fig. 8, the accumulation rate $a^{+}_{\mathrm{sat},0}$, the maximum surface velocity $v_{\mathrm{s,max}}$ and the maximum basal temperature relative to pressure melting $T'_{\mathrm{b,max}}$ are displayed for the simulation series with varied dust content. It is striking that the impact of the varied dust content on $a^{+}_{\mathrm{sat},0}$ is much larger than that of the flow law, its range being almost 30% of the value of run REF. Since the flow velocities are still small, this cannot be due to changes in the ice dynamics. The reason for the distinct increase of $a^{+}_{\mathrm{sat},0}$ with the dust content φ is rather that the more dust is present, the larger the density of the composite material becomes [Eq. (13)]. This entails a larger isostatic downward displacement of the underlying lithosphere, so that more ice needs to be accumulated in order to reach the target surface elevation of $h_{\mathrm{max}} = -1.95$ km.

It is very interesting that $v_{\mathrm{s,max}}$ also increases with increasing dust content, even though the direct effect on ice fluidity works in the opposite direction [Eq. (16)]. This is so because of two further, indirect effects, which outweigh direct hardening: (i) the above-mentioned increasing ice thickness which produces larger driving stresses, and (ii) the increasing basal temperature which makes the ice softer. The latter varies quite strongly, from $T'_{\mathrm{b,max}} = -67.2$°C for run REF dust to -52.4°C for run PHI50. This is mainly due to the decreasing heat conductivity [Eq. (14)] which leads to a stronger insulation of the ice body to the cold atmosphere. Nevertheless, even the highest temperature of run

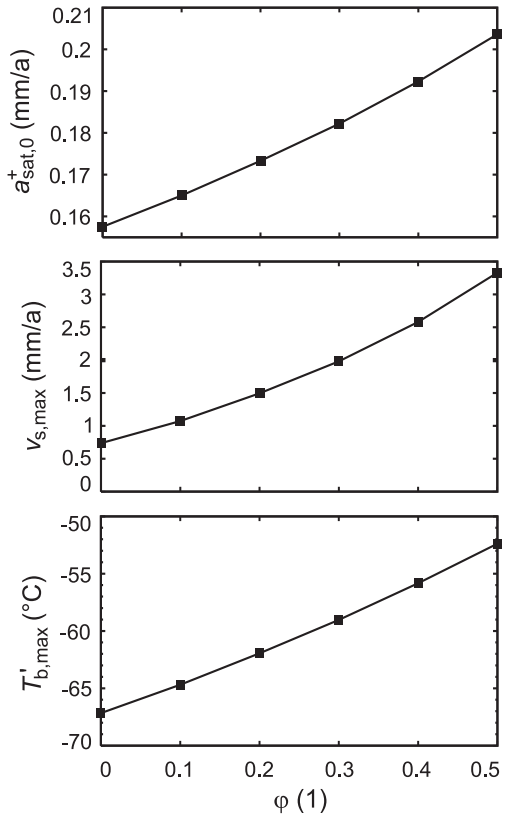

Figure 8: Dependency of the accumulation rate $a^+_{\mathrm{sat},0}$, the maximum surface velocity $v_{\mathrm{s,max}}$ and the maximum basal temperature relative to pressure melting $T'_{\mathrm{b,max}}$ on the dust content (Glen's flow law applied).

PHI50 is still far below the melting point, so that the presence of liquid water at the base of the NPC is very unlikely. The current position of the melting isotherm is expected to lie several kilometers deeper in the ground (see also Clifford et al. 2000).

7 Discussion

The simulations of this study provide a plausible scenario for the evolution of the NPC during the last five million years. With the simple climate forcing described in Sect. 2.2 it is possible to build up the NPC starting from ice-free initial conditions with an accumulation rate that is within the range of current estimates. Since the absolute values of ice-flow velocities are small for all investigated cases, the topography evolution is mainly controlled by the surface mass balance, and internal ice dynamics plays only a minor role.

Owing to the uncertainties of the applicable flow law, the dust content and the grain size, ice-flow velocities can only be predicted within a range of two orders of magnitude. Most likely present values are of the order of 0.1–1 mm a^{-1}, and a very

significant variation over climatic cycles can be expected. Further uncertainties which have not been treated here arise due to the possible presence of some amounts of CO_2 ice and CO_2 clathrate hydrate. Due to its low strength, CO_2 ice can occur only in small amounts. Otherwise the NPC would develop a very fast ice flow, which is not consistent with the existence of steep scarps and troughs in the ice and would ultimately bring the whole ice mass to a collapse. This statement is equally valid for the SPC (Durham et al. 1999, Nye et al. 2000). By contrast, CO_2 clathrate hydrate, which is thermodynamically stable in the interior of both polar caps (Jöns 2002, and references therein), has a very strong rheology. Based on laboratory measurements on CH_4 clathrate hydrate (Stern et al. 1996, Durham et al. 2003), it is estimated that CO_2 hydrate is at least an order of magnitude harder than pure H_2O ice at fixed stress and temperature (Durham 1998). In a similar fashion as for the dust discussed in Sect. 6, this direct hardening effect would probably be compensated or even over-compensated by the very low thermal conductivity of clathrate hydrates (Cook and Leaist 1983).

Nye (2000) assumed that the NPC (and also the SPC) is an ice body which collapses and spreads outward by flow in the course of time without significant accumulation and ablation, and solved the flow equations by applying a modified form of the similarity solution by Halfar (1983) for radial flow. The G & K flow law with $d = 1$ mm was chosen. In this conceptual glaciological approach, the topography evolution is governed by glacial flow only, whereas our results suggest that surface mass balance is the major influencing factor. Nevertheless, the reported creep rates for the present cap agree well with our findings. The age of the NPC, which is defined as the time the ice cap requires to reach the present height when starting from an initial state with asymptotically infinite height in Nye's (2000) study, cannot be compared directly to our build-up time which assumes an ice-free initial state. Still, the reported age of about 10 Ma is in the same range as our build-up time of 5 Ma inferred from climatological reasonings.

While the overall shape of the NPC can be reproduced well with the large-scale approach of this study, a more detailed investigation of structures like the spiralling scarps and troughs and their impact on the ice dynamics is not possible. Fisher (1993) suggested that ice accumulates on the white, flat areas, but evaporates on the south-facing dark scarps ("accublation" model). This mechanism keeps the scarps and troughs open; otherwise they would close due to ice flow on time-scales of 10^5 to 10^6 years, as it was demonstrated by Hvidberg (2003), Hvidberg and Zwally (2003). This entails a significant influence of the scarps and troughs on the local flow field with strongly enhanced ice-flow velocities of up to $50\,\mathrm{mm\,a^{-1}}$ at the steepest scarps, an effect that is neglected in our study. Therefore, our finding that the large-scale build-up process is essentially independent of glacial flow does not hold anymore for the evolution of these

smaller-scale structures.

Further, our assumption of a spatially and temporally constant dust content is a simplification of the real conditions. Imagery from orbiting spacecraft shows alternating layers of lighter and darker material for both polar caps, which consist most likely of ice with varying amounts of dust and may reflect climatic cycles (Clifford et al. 2000, and references therein). Rheologically, this leads to a sequence of weaker and harder layers within the ice body which experience different shear rates and may produce flow instabilities like folding and boudinage (Kargel and Tanaka 2002). However, these effects are of small-scale nature, and the large-scale flow for the whole ice body should still be prescribed well by averaging them out over larger distances.

Future work will encompass an improved coupling between the atmosphere and the ice cap by downscaling simulation results obtained with the atmosphere model PUMA-2 (Portable University Model of the Atmosphere, Fraedrich et al. 2003; see also `http://puma.dkrz.de/puma/`) adapted to Martian conditions (Segschneider et al. 2005). This will further improve the physical basis of the parameterizations for the surface temperature and the accumulation-ablation rate. Moreover, we will extend our investigations to the south-polar cap which probably has a very different history and dynamics than its counterpart in the north (Clifford et al. 2000).

Acknowledgements

We thank W. B. Durham and an anonymous referee for their comments on the paper. The scientific editor was P. C. Thomas. This work was supported by the Priority Programme 1115 “Mars and the Terrestrial Planets” of the German Research Foundation (Deutsche Forschungsgemeinschaft, DFG) under project nos. KE 226/8, GR 1557/4.

References

Byrne, S. and B. C. Murray. 2002. North polar stratigraphy and the paleo-erg of Mars. *J. Geophys. Res.*, **107** (E6), 5044. doi:10.1029/2001JE001615.

Clifford, S. M., D. Crisp, D. A. Fisher, K. E. Herkenhoff, S. E. Smrekar, P. C. Thomas, D. D. Wynn-Williams, R. W. Zurek, J. R. Barnes, B. G. Bills, E. W. Blake, W. M. Calvin, J. M. Cameron, M. H. Carr, P. R. Christensen, B. C. Clark, G. D. Clow, J. A. Cutts, D. Dahl-Jensen, W. B. Durham, F. P. Fanale, J. D. Farmer, F. Forget, K. Gotto-Azuma, R. Grard, R. M. Haberle, W. Harrison, R. Harvey, A. D. Howard, A. P. Ingersoll, P. B. James, J. S. Kargel, H. H. Kieffer, J. Larson, K. Lepper, M. C. Malin, D. J. McCleese, B. Murray, J. F. Nye, D. A. Paige, S. R. Platt, J. J. Plaut, N. Reeh, J. W. Rice, D. E. Smith, C. R. Stoker,

K. L. Tanaka, E. Mosley-Thompson, T. Thorsteinsson, S. E. Wood, A. Zent, Z. M. T. and Z. H. J. 2000. The state and future of Mars polar science and exploration. *Icarus*, **144** (2), 210–242.

Cook, J. G. and D. G. Leaist. 1983. An exploratory study of the thermal conductivity of methane hydrate. *Geophys. Res. Lett.*, **10** (5), 397–399.

Durham, W. B. 1998. Factors affecting the rheologic properties of Martian polar ice. In: *First International Conference on Mars Polar Science and Exploration*, LPI Contribution No. 953, pp. 8–9. Lunar and Planetary Institute, Houston, Texas, USA.

Durham, W. B., S. H. Kirby and L. A. Stern. 1997. Creep of water ices at planetary conditions: A compilation. *J. Geophys. Res.*, **102** (E7), 16293–16302.

Durham, W. B., S. H. Kirby and L. A. Stern. 1999. Steady-state flow of solid CO_2: Preliminary results. *Geophys. Res. Lett.*, **26** (23), 3493–3496.

Durham, W. B., L. A. Stern and S. H. Kirby. 2003. Ductile flow of methane hydrate. *Can. J. Phys.*, **81** (1-2), 373–380.

Fisher, D. A. 1993. If Martian ice caps flow – ablation mechanisms and appearance. *Icarus*, **105** (2), 501–511.

Fisher, D. A., D. P. Winebrenner and H. Stern. 2002. Lineations on the "white" accumulation areas of the residual northern ice cap of Mars: Their relation to the "accublation" and ice flow hypothesis. *Icarus*, **159** (1), 39–52.

Fraedrich, K., E. Kirk, U. Luksch and F. Lunkeit. 2003. Ein Zirkulationsmodell für Forschung und Lehre. *Promet*, **29** (1-4), 34–48.

Goldsby, D. L. and D. L. Kohlstedt. 1997. Grain boundary sliding in fine-grained ice I. *Scripta Materialia*, **37** (9), 1399–1406.

Greve, R. 2000a. *Large-scale glaciation on Earth and on Mars.* Electronic Publications Darmstadt No. 816, http://elib.tu-darmstadt.de/diss/000816/. Habilitation thesis, Department of Mechanics, Darmstadt University of Technology, Germany.

Greve, R. 2000b. Waxing and waning of the perennial north polar H_2O ice cap of Mars over obliquity cycles. *Icarus*, **144** (2), 419–431. doi:10.1006/icar.1999.6291.

Greve, R., V. Klemann and D. Wolf. 2003. Ice flow and isostasy of the north polar cap of Mars. *Planet. Space Sci.*, **51** (3), 193–204. doi:10.1016/S0032-0633(02)00206-4.

Greve, R., R. A. Mahajan, J. Segschneider and B. Grieger. 2004. Evolution of the north-polar cap of Mars: a modelling study. *Planet. Space Sci.*, **52** (9), 775–787. doi: 10.1016/j.pss.2004.03.007.

Halfar, P. 1983. On the dynamics of the ice sheets. 2. *J. Geophys. Res.*, **88** (C10), 6043–6051.

Hammer, C. U., H. B. Clausen, W. Dansgaard, A. Neftel, P. Kristinsdottir and E. Johnson. 1985. Continuous impurity analysis along the Dye 3 deep core. In: C. C. Langway, H. Oeschger and W. Dansgaard (Eds.), *Greenland Ice Core: Geophysics, Geochemistry and the Environment*, Geophysical Monographs No. 33, pp. 90–94. American Geophysical Union, Washington DC.

Hutter, K. 1983. *Theoretical Glaciology; Material Science of Ice and the Mechanics of Glaciers and Ice Sheets*. D. Reidel Publishing Company, Dordrecht, The Netherlands.

Hvidberg, C. S. 2003. Relationship between topography and flow in the north polar cap on Mars. *Ann. Glaciol.*, **37**, 363–369.

Hvidberg, C. S. and H. J. Zwally. 2003. Sublimation of water from the north polar cap of Mars. Abstract, Workshop "Mars Atmosphere Modelling and Observations", Granada, Spain, 13–15 Jan. 2003.

Jakosky, B. M., B. G. Henderson and M. T. Mellon. 1993. The Mars water cycle at other epochs: Recent history of the polar caps and layered terrain. *Icarus*, **102**, 286–297.

Johnson, C. L., S. C. Solomon, J. W. Head, R. J. Phillips, D. E. Smith and M. T. Zuber. 2000. Lithospheric loading by the northern polar cap on Mars. *Icarus*, **144** (2), 313–328.

Jöns, H.-P. 2002. Young/recent non-eolian exogenic dynamics on Mars: Large-scale influence by decomposition of CO_2 hydrates? *Z. Geol. Wiss.*, **30** (6), 403–421.

Kargel, J. S. and K. L. Tanaka. 2002. The Martian south polar cap: Glacial ice sheet of multiple interbedded ices. Abstract, 33rd Lunar and Planetary Science Conference, League City, Texas, 11–15 March 2002.

Laskar, J., B. Levrard and J. F. Mustard. 2002. Orbital forcing of the martian polar layered deposits. *Nature*, **419** (6905), 375–377.

Morland, L. W. 1984. Thermo-mechanical balances of ice sheet flows. *Geophys. Astrophys. Fluid Dyn.*, **29**, 237–266.

Nye, J. F. 1953. The flow law of ice from measurements in glacier tunnels, laboratory experiments and the Jungfraufirn borehole experiments. *Proc. R. Soc. Lond.*, **A219**, 477–489.

Nye, J. F. 2000. A flow model for the polar caps of Mars. *J. Glaciol.*, **46** (154), 438–444.

Nye, J. F., W. B. Durham, P. M. Schenk and J. M. Moore. 2000. The instability of a south polar cap on Mars composed of carbon dioxide. *Icarus*, **144** (2), 449–455.

Paterson, W. S. B. 1994. *The Physics of Glaciers.* Pergamon Press, Oxford etc., 3rd ed.

Rigsby, G. P. 1958. Effect of hydrostatic pressure on velocity of shear deformation of single ice crystals. *J. Glaciol.*, **3** (24), 273–278.

Segschneider, J., B. Grieger, H. U. Keller, F. Lunkeit, E. Kirk, K. Fraedrich, A. Rodin and R. Greve. 2005. Response of the intermediate complexity Mars Climate Simulator to different obliquity angles. *Planet. Space Sci.*, **53** (6), 659–670. doi:10.1016/j.pss.2004.10.003.

Smith, D. E., M. T. Zuber, S. C. Solomon, R. J. Phillips, J. W. Head, J. B. Garvin, W. B. Banerdt, D. O. Muhleman, G. H. Pettengill, G. A. Neumann, F. G. Lemoine, J. B. Abshire, O. Aharonson, C. D. Brown, S. A. Hauck, A. B. Ivanov, P. J. McGovern, H. J. Zwally and T. C. Duxbury. 1999. The global topography of Mars and implications for surface evolution. *Science*, **284** (5419), 1495–1503.

Stern, L. A., S. H. Kirby and W. B. Durham. 1996. Peculiarities of methane clathrate hydrate formation and solid-state deformation, including possible superheating of water ice. *Science*, **273** (5283), 1843–1848.

Thomas, P., S. Squyres, K. Herkenhoff, A. Howard and B. Murray. 1992. Polar deposits of Mars. In: H. H. Kieffer, B. M. Jakosky, C. W. Snyder and M. S. Matthews (Eds.), *Mars*, pp. 767–795. University of Arizona Press, Tucson.

Thorsteinsson, T. 1996. *Textures and fabrics in the GRIP ice core, in relation to climate history and ice deformation.* Reports on Polar Research No. 205. Alfred Wegener Institute for Polar and Marine Research, Bremerhaven.

van der Veen, C. J. 1999. *Fundamentals of Glacier Dynamics.* A. A. Balkema, Rotterdam.

Zuber, M. T., D. E. Smith, S. C. Solomon, J. B. Abshire, R. S. Afzal, O. Aharonson, K. Fishbaugh, P. G. Ford, H. V. Frey, J. B. Garvin, J. W. Head, A. B. Ivanov, C. L. Johnson, D. O. Muhleman, G. A. Neumann, G. H. Pettengill, R. J. Phillips, X. Sun, H. J. Zwally, W. B. Banerdt and T. C. Duxbury. 1998. Observations of the north polar region of Mars from the Mars Orbiter Laser Altimeter. *Science*, **282** (5396), 2053–2060.